

The Sloan Digital Sky Survey Reverberation Mapping Project: the XMM-Newton X-Ray Source Catalog and Multiband Counterparts

Teng Liu (刘腾)¹, Andrea Merloni¹, Torben Simm¹, Paul J. Green², William N. Brandt³,⁴,⁵, Donald P. Schneider³,⁴, Tom Dwelly¹, Mara Salvato¹, Johannes Buchner¹, Yue Shen^{6,7}, Kirpal Nandra¹, Antonis Georgakakis⁸, and Luis C. Ho^{9,10}

Max-Planck-Institut für Extraterrestrische Physik, Giessenbachstraße 1, D-85748 Garching bei München, Germany; lewtonstein@gmail.com
 ² Harvard-Smithsonian Center for Astrophysics, MS-4 60 Garden St., Cambridge, MA 02138, USA
 ³ Department of Astronomy & Astrophysics, 525 Davey Lab, The Pennsylvania State University, University Park, PA 16802, USA
 ⁴ Institute for Gravitation and the Cosmos, The Pennsylvania State University, University Park, PA 16802, USA
 ⁵ Department of Physics, 104 Davey Lab, The Pennsylvania State University, University Park, PA 16802, USA
 ⁶ Department of Astronomy, University of Illinois at Urbana-Champaign, Urbana, IL 61801, USA
 ⁷ National Center for Supercomputing Applications, University of Illinois at Urbana-Champaign, Urbana, IL 61801, USA
 ⁸ Institute for Astronomy and Astrophysics, National Observatory of Athens, V. Paulou & I. Metaxa, 11532, Greece
 The Kavli Institute for Astronomy and Astrophysics, Peking University, 5 Yiheyuan Road, Haidian District, Beijing, 100871, People's Republic of China Received 2020 May 16; revised 2020 August 14; accepted 2020 September 1; published 2020 October 9

Abstract

The XMM-RM project was designed to provide X-ray coverage of the Sloan Digital Sky Survey Reverberation Mapping (SDSS-RM) field. Forty-one XMM-Newton exposures, placed surrounding the Chandra AEGIS field, were taken, covering an area of 6.13 deg² and reaching a nominal exposure depth of ~15 ks. We present an X-ray catalog of 3553 sources detected in these data, using a PSF-fitting algorithm and a sample selection threshold that produces a ~5% fraction of spurious sources. In addition to the PSF-fitting likelihood, we calculate a second source reliability measure based on Poisson theory using source and background counts within an aperture. Using the Poissonian likelihood, we select a subsample with a high purity and find that it has number count profiles similar to previous X-ray surveys. The Bayesian method "NWAY" was employed to identify counterparts of the X-ray sources from the optical Legacy and the IR unWISE catalogs, using a two-dimensional unWISE magnitude–color prior created from optical/IR counterparts of Chandra X-ray sources. A significant number of the optical/IR counterparts correspond to sources with low detection likelihoods, proving the value of retaining the low-likelihood detections in the catalog. A total of 932 of the XMM-RM sources are covered by SDSS spectroscopic observations, where 89% of them are classified as active galactic nuclei, and 71% of these active galactic nuclei are in the SDSS-RM quasar catalog. Among the SDSS-RM quasars, 80% are detectable at the depth of the XMM observations.

Unified Astronomy Thesaurus concepts: Astronomy data analysis (1858); Supermassive black holes (1663); Active galactic nuclei (16); X-ray active galactic nuclei (2035); Quasars (1319); X-ray point sources (1270)

Supporting material: tar.gz file

1. Introduction

The Sloan Digital Sky Survey Reverberation Mapping (SDSS-RM) project (Shen et al. 2015, 2019) is the first multiobject RM program with the aim of measuring the black hole masses of a large representative quasar sample at cosmological distances. This project focuses on a single 7 deg² field centered around 213°.7, 53°.1 (J2000), in which 849 broad-line quasars with $i_{\rm psf}({\rm SDSS}) < 21.7$ mag and 0.1 < z < 4.5 were selected and continuously monitored with the BOSS spectrographs (Smee et al. 2013), first within the SDSS-III (Eisenstein et al. 2011; Dawson et al. 2013) and then within the SDSS-IV (Blanton et al. 2017) programs, forming a unique sample of quasars with unprecedented multiband, multiepoch imaging and spectroscopy. The field is fully covered by the Panoramic Survey Telescope and Rapid Response System (Pan-STARRS) Medium Deep Field survey (Kaiser et al. 2010; Tonry et al. 2012), the WISE survey (Wright et al. 2010; Lang et al. 2016), and the Faint Images of the Radio Sky at Twenty cm (FIRST) radio survey (White et al. 1997). It is also covered partially by the Galaxy Evolution Explorer (GALEX) near-ultraviolet survey (Gezari et al. 2013), United Kingdom Infrared Telescope near-infrared imaging, and

the All-wavelength Extended Groth strip International Survey (AEGIS; Davis et al. 2007). Since the X-ray band is of particular importance to the study of active galactic nuclei (AGNs), as it provides important information about the AGN environment near the black hole, we initiated the XMM-RM project to survey this field in the X-ray band with XMM-Newton. This paper presents the X-ray catalog and optical/IR counterparts of the X-ray sources in this field. The WMAP cosmology with $\Omega_m = 0.272$, $\Omega_{\Lambda} = 0.728$, and $H_0 = 70.4$ km s⁻¹ Mpc⁻¹ (Komatsu et al. 2011) is adopted.

2. Observations and Data Reduction

2.1. The Data

The XMM-Newton observations cover a total sky area of ${\sim}6.13\,\text{deg}^2$ within the $7\,\text{deg}^2$ RM field. The main data set is formed by 41 XMM observations with individual exposure times of ${\sim}15$ ks, with 13 pointings obtained in AO15 (PI P. Green) and 28 in AO16 (PI A. Merloni). All observations were taken in full-frame mode of the EPIC-PN/MOS cameras. Most observations were performed with the thin filter; only four observations

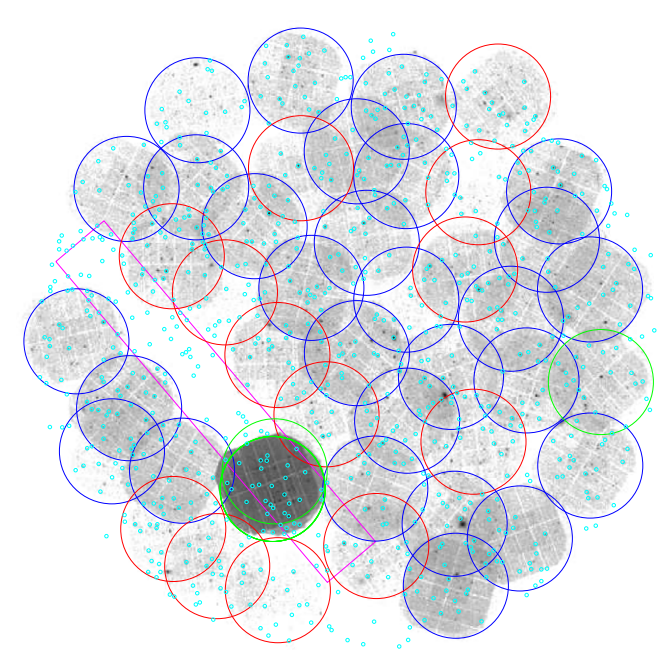


Figure 1. X-ray (0.5-7.5 keV) mosaic image of all XMM observations with XMM pointings (30') diameter circles) and RM quasar positions (cyan points). Red and blue circles indicate the 13+28 pointings from AO15 and AO16, respectively. Green circles correspond to existing archival XMM observations. The magenta box is the Chandra AEGIS/EGS field.

required the medium filter because of nearby bright field stars. The footprint of the XMM-RM survey is shown in Figure 1. The pointings have a regular 22' spacing and overlap sufficiently to provide a uniform coverage of sensitivity.

In addition to these XMM-RM dedicated observations, we also reanalyze seven archival XMM observations in the RM field (see Figure 1), including five Groth-Westphal Strip observations (PI R. Griffiths) and two object-targeted observations (0503960101, PI M. Agueros; 0723860101, PI D. Lin). Two observations (0127920401, 0127920901) are excluded because of high background flaring during the exposures. In total, 90% (756/849) of the SDSS-RM quasars are covered by the XMM observations. Table 1 lists the details of the XMM observations presented in this work.

The Extended Groth Strip (EGS, ~0.67 deg²), which is located within the SDSS-RM field (see Figure 1), was observed by Chandra. The entire EGS is covered to a depth of 200 ks, while the central 0.29 deg² reaches a nominal depth of 800 ks as part of the AEGIS-X Deep survey. These observations are described in Nandra et al. (2005), Laird et al. (2009), Goulding et al. (2012), and Nandra et al. (2015), with the X-ray source catalogs and the corresponding multiband counterparts presented. This paper focuses only on the XMM data.

2.2. Data Processing

The data processing was performed with the XMM-Newton Science Analysis Software (SAS) version 18.0.0 (Gabriel et al. 2004). Aiming to optimize the sensitivity for faint point sources, we developed a dedicated data-reduction strategy to suppress noise.

The first step is the creation of EPIC PN and MOS event files from the Observation Data Files (ODF) by executing the EPCHAIN and EMCHAIN SAS tasks. In addition to the standard event file, we also create an out-of-time (OOT) event file for

the PN data. To avoid spurious detections at the CCD edges, we remove the pixels along the edges of the PN and MOS CCDs by flagging them as dead pixels. For the PN, we exclude events with patterns larger than 4 or with energies in the ranges of instrument lines (Ranalli et al. 2015), that is, 1.39–1.55 keV (Al) and 7.35-7.60, 7.84-8.28, 8.54-9.00 keV (Cu). We adopt a stricter event flag filter than the commonly used "XMMEA_EP," excluding the "CLOSE_TO_CCD_BORDER," "CLOSE_TO_ CCD WINDOW," "OUT OF FOV," and "OUT OF CCD WINDOW" events (flag code 0xefb0006). At energies below 1 keV, we also reject "ON OFFSET COLUMN" events (0xefb000e). For the MOS, we exclude events with patterns larger than 12 or with energies in the ranges of 1.39-1.55 keV (Al) and 1.69-1.80 keV (Si). In addition to the commonly used "XMMEA_EM" filter, we also exclude the "CLOSE_TO_ CCD BORDER" and "CLOSE TO CCD WINDOW" events (0x766ba006).

We adopt a two-step procedure to reject background flares. First, strong flares are excluded using the espfilt "ratio" method in the 8-12 keV band, allowing a count rate ratio of inside to outside the field of view (FOV) of 1.5. Excluding such flares, images and exposure maps are constructed in the 0.5-7.5 keV band, and sources are detected using eboxdetect. Then, a lightcurve is extracted from the source-free region in the 0.5-7.5 keV band, which is the band used for source detection in this work. We use bkgoptrate to find the count rate threshold at which the maximum signal-to-noise ratio (S/N) is achieved after excluding the bins above the threshold. This threshold defines cleaner good time intervals (GTIs). Finally, we merge all GTIs generated by ep/ emchain for each CCD and the GTIs from espfilt and from bkgoptrate using the "AND" mode. The MOS1 and MOS2 lightcurves are merged before running bkgoptrate, and only one final GTI was constructed for MOS1 and MOS2. In Table 1, the cleaned exposure times are listed and also expressed as percentages of the raw exposure time.

2.3. Astrometric Correction

Initially, we run source detection as described in Section 3 in the full band without any astrometric correction. For each observation, we compare the detected sources with an optical/ IR reference catalog created by Rosen et al. (2016) based on the SDSS, 2MASS, and USNO-B1.0 catalogs, using the task catcorr, which calculates both the shift and rotation corrections and the corresponding errors. The shift is typically <0.15. We apply the corrections to the attitude file and reconstruct the event files using the task evproject. The analyses hereafter are based on these astrometrically corrected event files. After source detection, we convert the errors of the corrections into an additional systematic error for each source (the "SYSERRCC" column in the catalog) according to its off-axis angle. In the final catalog, one source could be detected in multiple observations, which contribute different systematic errors. We choose the largest one for simplicity.

3. Source Detection

3.1. Images

Three energy bands are used for source detection: full (0.5–7.5 keV), soft (0.5–2 keV), and hard (2–7.5 keV). A pixel scale of 4" is used. In order to improve the measurement of the background, which is essential to the detection of faint sources, we also create filter-wheel-closed (FWC) background maps and

Table 1
XMM-RM Observations

ObsID	R.A. (deg)	Decl. (deg)	DATE	PN MODE	PN T _{EXP} (ks (%))	MOS MODE	MOS T _{EXP} (ks (%))
0127921001	214.3060	52.3726	2000-07-21	EFF-Thin	45(87)	FF-Thin	53.1(95)
0127921201	214.3045	52.3725	2000-07-23	EFF-Thin	14.4(98)	FF-Thin	18.4(99)
0127921101	214.3044	52.3725	2000-07-23	EFF-Thin	3.6(97)	FF-Thin	7.5(100)
0503960101	211.7222	52.8577	2007-06-21	FF-Thin	12.7(53)	FF-Thin	18(68)
0723860101	214.2908	52.4564	2014-01-05			FF-Thin	20.3(71)
0765070301	212.4808	54.2289	2015-12-24	FF-Thin	13.2(83)	FF-Thin	15.8(90)
0762500301	213.5022	52.1000	2015-12-26	FF-Thin	10.7(72)	FF-Thin	13.7(83)
0762500201	214.6906	53.3064	2015-12-26	FF-Thin	2.8(18)	FF-Thin	6.4(37)
0762500901	214.2633	51.8914	2016-01-13	FF-Thin	3.4(21)	FF-Thin	8.4(48)
0762500501	213.8848	52.7277	2016-01-15	FF-Thin	4.3(27)	FF-Thin	13.3(76)
0765080101	214.0848	53.8985	2016-01-21	FF-Thin	5(25)	FF-Thin	11.7(52)
0765080801	215.0757	52.1784	2016-01-23	FF-Medium	5.2(31)	FF-Medium	8.4(45)
0765090801	212.6571	53.7758	2016-01-23	FF-Thin	4.5(30)	FF-Thin	6.7(40)
0765081001	212.7749	53.4096	2016-01-27	FF-Thin	11.1(79)	FF-Medium	15.4(99)
0765080601	212.7343	52.5897	2016-01-27	FF-Thin	10.4(95)	FF-Thin	12.6(100)
0765080901	214.7323	52.0041	2016-01-27	FF-Thin	3.2(29)	FF-Medium	12.6(100)
0762500401	214.2715	53.0097	2016-01-31	FF-Thin	10.6(66)	FF-Thin	15.5(88)
0762500101	215.1179	53.4753	2016-02-02	FF-Thin	12.1(95)	FF-Thin	14.3(99)
0804270101	214.0023	53.3293	2017-05-09	FF-Thin	17.4(92)	FF-Thin	20.6(100)
0804270201	214.0879	54.3156	2017-05-10	FF-Thin	13.7(98)	FF-Thin	15.6(100)
0804270601	212.8912	51.9066	2017-05-11	FF-Thin	9.1(48)	FF-Thin	20.6(100)
0804270401	212.0070	53.7704	2017-05-19	FF-Thin	15.5(82)	FF-Thin	17(83)
0804270501	213.5061	52.3733	2017-05-20	FF-Thin	11(79)	FF-Thin	15.3(98)
0804270301	213.2358	53.8581	2017-05-24	FF-Thin	12.7(98)	FF-Thin	13.2(100)
0804270701	215.4901	53.7919	2017-05-24	FF-Thin	13.7(99)	FF-Thin	15.5(100)
0804270901	215.0135	52.4560	2017-05-29	FF-Thin	18.1(95)	FF-Thin	20.6(100)
0804270801	211.8265	52.4625	2017-05-30	FF-Thin	14.8(99)	FF-Thin	16.6(100)
0804271301	213.6429	53.0179	2017-06-08	FF-Thin	18.5(97)	FF-Thin	20.6(100)
0804271401	213.2518	52.6945	2017-06-09	FF-Thin	13.5(96)	FF-Medium	15.4(99)
0804271501	212.8926	52.2013	2017-06-09	FF-Thin	13.5(96)	FF-Thin	15.1(97)
0804271001	215.4357	52.7492	2017-06-12	FF-Thin	17.9(94)	FF-Thin	20.6(100)
0804271201	214.4570	53.6221	2017-06-13	FF-Thin	12.8(91)	FF-Thin	15.6(100)
0804271101	214.9297	53.8047	2017-06-13	FF-Thin	13.4(96)	FF-Thin	15.6(100)
0804271601	212.3896	52.1253	2017-07-14	FF-Thin	7.5(41)	FF-Thin	14.8(74)
0804271901	212.9022	52.8998	2017-07-15	FF-Thin	13.2(94)	FF-Thin	15.6(100)
0804271701	213.5579	53.5425	2017-07-20	FF-Thin	8.2(49)	FF-Thin	13.6(72)
0804272101	213.6338	53.9783	2017-07-22	FF-Thin	4.4(24)	FF-Thin	5.7(34)
0804272301	215.8629	53.0618	2017-07-23	FF-Thin	11(79)	FF-Thin	15.5(99)
0804272501	213.2493	54.1879	2017-07-23	FF-Thin	13.5(96)	FF-Thin	15.6(100)
0804272801	214.9270	54.1715	2017-07-24	FF-Thin	6.7(38)	FF-Thin	8(43)
0804271801	213.2472	53.2703	2017-11-09	FF-Thin	6(45)	FF-Thin	6.4(56)
0804272201	212.3076	52.8757	2017-11-15	FF-Thin	13.3(95)	FF-Thin	15.3(98)
0804272001	215.5636	52.5425	2017-11-16	FF-Thin	10.4(72)	FF-Thin	4.1(91)
0804272401	212.4188	53.1708	2017-11-27	FF-Thin	12.3(88)	FF-Thin	14.9(96)
0804272601	212.1157	53.5421	2017-11-27	FF-Thin	13.6(97)	FF-Thin	15.4(99)
0804272701	211.7837	53.2997	2017-12-03	FF-Thin	18.7(98)	FF-Thin	20.7(100)

Note. Column 1: XMM observation ID; columns 2–3: aim point (J2000); column 4: observation date; columns 5, 7: observation mode and filter for PN and MOS (FF for PrimeFullWindow and EFF for PrimeFullWindowExtended); columns 6, 8: cleaned exposure time ("ONTIME") after removal of background flares and its ratio to raw exposure time in percentage terms.

OOT maps (for PN only, also hereafter whenever OOT is mentioned) for each observation using the eimageget task. To increase the S/N of the FWC map while taking account of the long-term instrument variability, for each observing mode we divide all of the FWC observations obtained from 2001 to 2017 into five epochs, each one having approximately the same summed exposure time, and we merge the events in each epoch. We find that the stacked FWC map is highly flat and does not have a sufficient S/N to reveal any feature at the small point-spread function (PSF) scales. Since in this work we are particularly interested in faint point sources rather than

extended emission on large scales, we calculate the mean value of the FWC map at each epoch. These values are used in the subsequent analysis.

To construct the OOT map for PN, the OOT image is smoothed only along the CCD reading columns (DETY direction in detector coordinates), making a stripe-pattern image that assigns the same value to all of the pixels of each CCD with the same DETX.

We make the exposure maps using the expmap task with the highest positional accuracy (0.02) in order to match the sky coordinates of the images exactly.

3.2. Background Maps

We detect sources in each image by running <code>eboxdetect</code> twice with a box size of five pixels and a minimum likelihood of 8: the first iteration is in local mode (without background map), and the second uses the background map generated by <code>esplinemap</code> on the basis of the catalog detected in the first run. We exclude the detected sources using <code>esplinemap</code>. The removal of the source signal does not have to be perfect, because the residual source remnants can be excluded later through sigma clipping.

The source-removed image is adaptively smoothed to achieve an S/N of 10 using asmooth. The different convolvers used in different parts of the image are saved. The corresponding exposure map and OOT map are smoothed using the same convolvers, keeping them consistent with each other.

Subtracting the FWC flux and the smoothed OOT map from the smoothed image produces the X-ray background component, which, in principle, follows the vignetted exposure map; that is, the flux map generated by dividing the residual image by the vignetted exposure map should be flat. However, the vignetted exposure maps might not be perfectly accurate because (1) the vignetting maps, which are energy dependent, are generated at single typical energies of each band; (2) the soft-proton background component, which does not follow the same vignetting map as the X-ray photons, cannot be completely removed. Deviations will appear as a centrosymmetric pattern. Therefore, we model the flux map with a centrosymmetric model, a one-dimensional quadratic smoothing spline model as a function of off-axis angle, 11 and we calculate this spline with the values of all of the pixels. By iterative 3σ clipping, the potential remnants of source signals can be excluded. Finally, the background map is generated by adding the FWC flux and OOT map back to the spline-modeled background map.

Our background map is generated on the assumption that the X-ray background has a uniform flux across the FOV. This assumption can be violated if a large, extended X-ray source falls inside or nearby the FOV, but there is no such case in this field.

3.3. Simultaneous PSF-fitting Detection

It is common practice in XMM surveys to have large overlaps between nearby pointings, and ours is no exception. In overlapping regions, we have the possibility of increasing the detection sensitivity. However, the varying PSF across the EPIC FOV makes it a bad idea to stack the images, since the detailed PSF shapes, which differ in different observations, are lost during the stacking. In this work, we detect sources through simultaneous PSF fitting using the task emldetect on the images of each camera in each observation without stacking. In this approach, not only the data but also the PSF shapes ("ellbeta" model) at each position in each observation are fully exploited.

Due to limitations in the capabilities of emldetect, some special treatment of the images is needed. To avoid a large number of images being input to emldetect, we use a 4×4 grid to divide the entire field into smaller cells, each of which is covered by a few tens of images at most. For each cell, we create an image for each camera in each observation using the

same frame of the cell, adding a 36" padding region around the edges. The exposure maps, background maps, and detection masks are reprojected onto the same frame using the CIAO task reproject_image. We run emldetect on these images, producing a catalog for each cell. When we merge the catalogs of all of the cells, the padding (overlapping) regions are checked in order to avoid missing any source that is detected as being just outside the cell in all cases and to avoid any duplicate source that is detected by more than one cell as being inside the cell.

The PSF fitting is done within a radius of five pixels (20''). Multisource fitting is applied for sources located within 10 pixels of each other. The detection mask is chosen as the region where the full-band exposure time is at least 10% of the maximum in the FOV.

The PSF fitting provides a detection likelihood L, which is equivalent to the probability p for a random Poissonian fluctuation to have caused the observed source counts in terms of $L=-\ln(p)$. Note that for small numbers of source photon counts, this relation is only a rough estimation (Cash 1979). We selected a relatively low threshold of L>3, which corresponds to a nominal spurious fraction of 5%.

3.4. Independent Detections in Three Bands

Considering the variety of spectral shapes of X-ray sources, simply using the information in the full band does not always produce the best sensitivity. For very soft or very hard sources, using the data in only the soft or hard band could result in a higher S/N ratio. To account for this, we ran source detections independently in the full, soft, and hard bands and then merged the catalogs.

We match the sources detected in different bands as follows. First, the output sources of the PSF fitting in different bands triggered by the same input source are considered as one. Second, we allow a minimum source separation of 9", which is approximately the half-energy PSF radius of XMM EPIC at 1.5 keV. Taking the positional error into account, when the separation of two sources is less than 9" + $\sqrt{\sigma_{\text{Source1}}^2 + \sigma_{\text{Source2}}^2}$, we interpret them as a single object. This threshold will not likely cause any mismatches, considering that the minimum separation between full-band detected sources is ~ 12 ".

3.5. Three-pass Detections

Before running the PSF fitting software, we require an initial set of positions of candidate sources. For each cell, we stack all of the images, exposure maps, and background maps and feed them to the CIAO task wavdetect, using wavelet scales of 2, 3, 4, 6, 8, and 16 pixels and a threshold of 10^{-4} . This procedure results in a large seed catalog with many spurious sources. We merge the catalogs detected in the three bands and input the merged catalog to the next pass, emldetect.

Running PSF fitting on the raw catalog from wavdetect, we compile a catalog and select sources with a detection likelihood >3. This new list of sources is fed back to emldetect to repeat the PSF fitting. Since a large number of unrealistic, faint sources are removed from the input list, unnecessary multi-PSF fittings are prevented. Based on the second iteration of PSF fitting, we again select the sources with a detection likelihood >3, then merge the catalogs detected in each cell, and in a last step merge the catalogs in each energy

 $[\]overline{\mbox{11}}$ We make use of the <code>interpolate.LSQUnivariateSpline</code> function in the "scipy" package.

band. The final catalog contains 3553 sources. It is publicly available along with this paper and described in the Appendix.

3.6. Extended Sources

A source extent likelihood is calculated by emldetect as the likelihood difference between a fit of the source surface brightness with a beta model and that with the PSF model. A minimum extent likelihood of 5 is adopted. In the final catalog, there are only 19 sources with an extent likelihood >10. They are considered as extended sources. We remark that this small sample of extended sources is neither complete nor clean, because the detection and selection in this work are optimized for unresolved sources but not for extended sources. For example, the PSF fitting within a small region is inefficient at identifying diffuse emission; fitting an extended source with the PSF results in residual diffuse emission that may easily be misidentified as a group of faint sources, and bad columns of the CCD could affect the fitting and cause false extent classifications. A detailed study of galaxy clusters is outside the scope of this paper. We focus on unresolved sources, especially AGNs, which constitute a large majority of the X-ray sources in such an extragalactic field. We cross-correlate the sources that have an extent >0 or have an X-ray neighbor within 1' with the Wen et al. (2012) SDSS cluster catalog within a distance of 1.15, and we visually inspect the matches. Half (13) of the extent >0 sources can be associated with SDSS clusters. We also identify another 24 unresolved sources that are likely SDSS clusters misclassified as unresolved or likely substructures of the SDSS clusters. In total, these sources are attributed to 15 SDSS clusters. The corresponding cluster ID in the Wen et al. (2012) catalog is added in our catalog (the "SDSS_Cluster" column).

4. The XMM-RM Source Catalog

4.1. Average Flux

For each camera, we calculate the energy conversion factors (ECFs) from our full-, soft-, and hard-band count rates to 0.5–10, 0.5–2, and 2–10 keV fluxes, respectively, using the response files generated at the aim point of each camera, assuming an absorbed power-law model with a slope of 1.7 and Galactic absorption (HI4PI Collaboration et al. 2016). The narrow instrument-line bands, which are excluded when making the images, are also excluded here. With these ECFs, we convert the count rate of each source in each camera and each observation to flux.

In each observation, the single-epoch flux of each source is calculated by averaging among the cameras. When the PSF weighted on-chip fraction of one source is <0.8 in one camera, this detection is excluded from the flux calculation, because such detections often lie at the border of the FOV or in CCD gaps, where the calibration is inaccurate and the flux correction is less reliable. The average flux of each source is calculated as the exposure-time-weighted mean flux among the multiple observations. When the three cameras have different exposure times in one observation, the longest one is used. A source might have a flux of zero in one camera during one observation; such cases are not excluded in the flux averaging. The distribution of soft fluxes is shown in Figure 2, in comparison with the flux distributions of the C-COSMOS (Civano et al. 2016), Stripe 82 Chandra (LaMassa et al. 2016), and XMM-SERVS (Chen et al. 2018) catalogs.

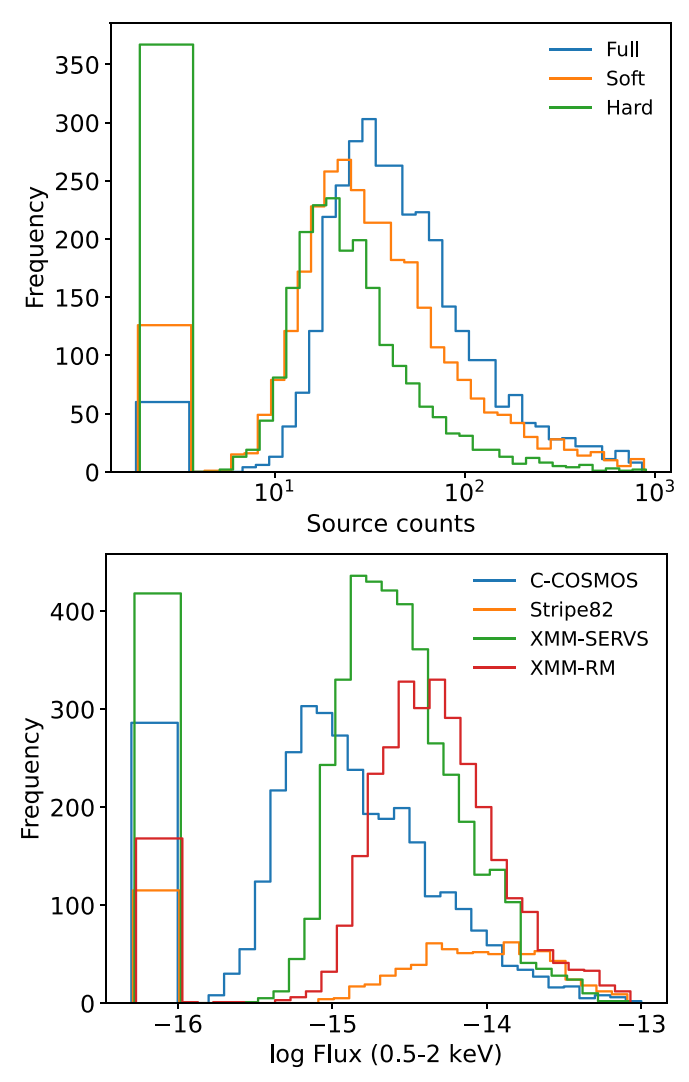


Figure 2. Distributions of source counts in the three bands (upper panel) and the 0.5–2 keV fluxes (lower panel) of the XMM-RM sources in comparison with the C-COSMOS and Stripe 82 Chandra surveys and the XMM-SERVS survey. Sources that are undetected and thus have zero counts and flux in a specific band are plotted in special bins at the lower end of the distribution, showing their number in terms of area in the histogram bins.

4.2. EEF Map and ECF Map

For each camera, we generate "ellbeta" PSF images using the task psfgen at a series of off-axis angles and calculate the 16" enclosed energy fraction (EEF) for them. As shown in Figure 3, at high off-axis angles, the EEF curve turns over and increases with off-axis angle, indicating the PSF model is suspect in such cases. Thus we exclude this increasing part. By interpolating and extrapolating the EEF as a function of off-axis angle, we build an EEF map for each camera in each observation. These EEF maps are stacked to create an EEF map for the whole field. The value at each position is calculated as the weighted mean of all the EEF maps covering this position. For the MOS cameras, we use the exposure maps as the weights, while for PN, we use the exposure map divided by 0.4, since the effective area of each MOS camera is about 0.4 of that of PN.

For each camera in each observation, we construct an ECF map by filling the FOV with the ECF of the camera. Each ECF map is multiplied by the corresponding vignetted exposure

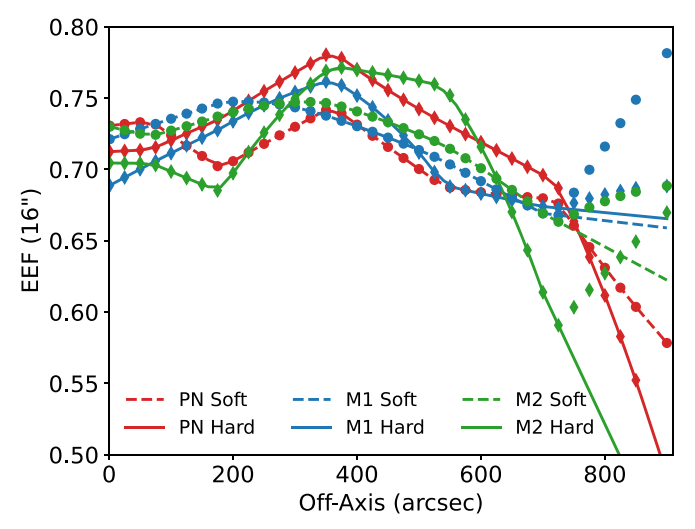


Figure 3. The 16'' enclosed energy fraction (EEF) as a function of off-axis angle. The lines are produced by the spline fitting. The increasing parts at large off-axis angles are excluded from the fitting.

map, creating an Exp-ECF map. Stacking all of them produces an Exp-ECF map for the entire field, which stores the conversion factor from source net counts to flux at each position. The stacked full-band EEF map and Exp-ECF map are presented in Figure 4.

4.3. Poissonian Likelihood and Sensitivity Map

In additional to the source-detection likelihood measured with PSF fitting, we calculate the Poissonian likelihood based on aperture source and background counts (Georgakakis et al. 2008). We apply the task eregionanalyses on the stacked images, background maps, and exposure maps to measure the source and background counts and count rates in a 16" radius (four pixels) circular aperture. For aperture source counts S and background counts B (note S+B is always an integer), the Poisson probability of the source being spurious is Poisson_B($\geqslant S + B$) = $\gamma(S + B, B)$, where γ is the regularized lower incomplete gamma function, and this probability is converted to a likelihood as $L = -\ln(p)$. In the case of blending with nearby sources, the aperture source counts are overestimated. To reject such contamination, when the distance of a source to its nearest neighbor is <32'', we replace the aperture source counts with that measured from PSF fitting, that is, the emldetect source counts multiplied by the EEF at the source position.

The two likelihoods can be significantly different in individual cases, as compared in Figure 5. At high likelihoods, the Poissonian likelihood is smaller than the PSF-fitting one. At low likelihoods, the Poissonian likelihood becomes relatively higher and comparable with the PSF-fitting one, but with a large scatter. In consideration of the large scatter, we remark that a PSF-fitting likelihood selected sample can be incomplete with respect to the Poissonian likelihood, as some sources that could survive the Poissonian likelihood threshold might be already removed during the PSF-fitting preselection. This is one of the reasons that we choose a PSF-fitting threshold as low as 3 when creating the XMM-RM catalog.

The Poissonian likelihood is not as good as the PSF-fitting likelihood in distinguishing source signal and fluctuations; however, a Poissonian-likelihood threshold can be straightforwardly converted to a map of flux limit in the field, that is, a

sensitivity map. We construct an aperture-background-counts map by convolving the background map with a 16" circular kernel filled with unity value. The value of background counts in this map is converted to a minimum source count in the aperture required to achieve a given likelihood, ¹² creating a map of aperture-source-counts limit (*M*). Dividing this map by the EEF map and the Exp-ECF map (Figure 4), we convert the minimum source count to flux in units of erg cm⁻² s⁻¹.

4.4. Sky Coverage and Number Counts

We employed two methods to calculate the number counts of the sources. The first one is a commonly used method (e.g., Cappelluti et al. 2009) that is called the "Simple" number counting method in this work. It simply sums the number of pixels that reach a given flux limit in the sensitivity map to calculate the sky coverage (Ω) as a function of flux, and then it sums the number of sources above a given likelihood threshold, with each source weighted by the reciprocal of the sky coverage at its flux (f):

$$N(>f) = \sum \frac{1}{\Omega_f}.$$
 (1)

The "Simple" sky coverage is shown in Figure 6 as solid lines, which are used to calculate sample flux limits. Adopting a Poissonian-likelihood threshold of 12, we find that the flux limits corresponding to a sky area of a circle of radius 12' (0.12 deg², approximately the size of the XMM FOV) are 1.7 \times 10 $^{-15}$ and 9.2 \times 10 $^{-15}$ erg cm $^{-2}$ s $^{-1}$ for the soft and hard bands, respectively, and the values corresponding to an area of 1 deg² are 2.6 \times 10 $^{-15}$ and 1.45 \times 10 $^{-14}$ erg cm $^{-2}$ s $^{-1}$, respectively. The second method—"Poisson" probability distribution

stacking—is more accurate than the "Simple" method as it takes into account the Poisson distribution of observed photon counts (Georgakakis et al. 2008). With a background aperture count B, let λ be the expected total aperture counts at a given flux $\lambda = f \cdot \text{Exp-ECF} \cdot \text{EEF} + B$. The conversion factors from fluxes to counts (Exp \cdot ECF \cdot ECF) are obtained from the corresponding maps in Figure 4. When converting the detection limit of aperture source counts M in each pixel of the sensitivity map into flux, it is converted to a flux probability distribution Poisson_{λ}($\geqslant M + B$) rather than a single flux limit. The flux distributions in all of the pixels are summed to calculate the sky coverage. As shown in Figure 6, such sky coverage curves (dashed) extend to lower fluxes than that using the "Simple" method (solid), since with this "Poisson" method, any source below the flux limit is considered as detectable with a certain probability. Likewise, when converting a source aperture count S to flux, it is converted to a flux probability distribution Poisson_{λ}(S + B)N(f) rather than a single flux. The factor N(f)is an empirical differential number count, which is applied in order to correct the Eddington bias. In this work, we adopt the best-fit broken power-law model of AGN number counts from the 7Ms CDFS survey (Luo et al. 2017). When summing the sources to calculate the logN-logS as in Equation (1), the number 1 of each source is replaced with the normalized flux probability distribution $P(f)df / \int P(f)df$.

It is common practice to use a clean sample with a high selection threshold to calculate the logN–logS. To limit the contamination in

 $[\]overline{\ }^{12}$ We make use of the special gammain coinv function of the "scipy" package.

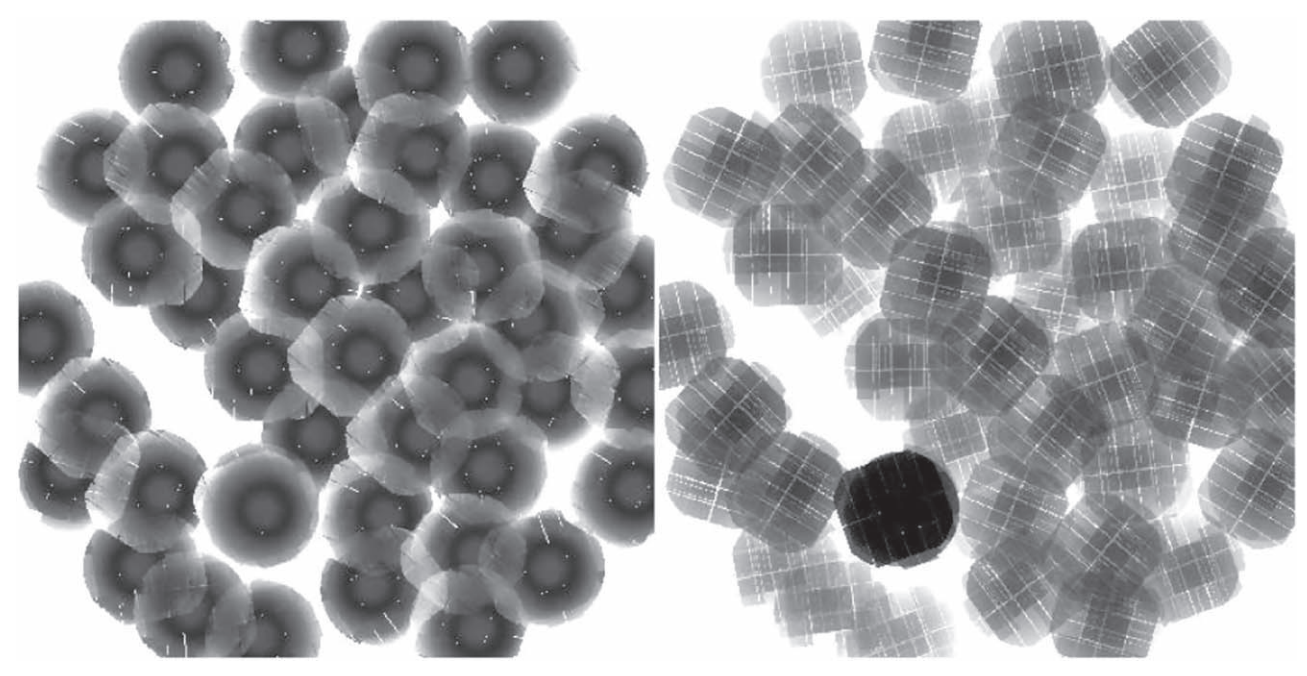


Figure 4. Full-band stacked enclosed energy fraction (EEF) map (left) and exposure × energy conversion factor (Exp-ECF) map (right). A darker color indicates a higher value.

the sample to 1%, a common choice of Poissonian-likelihood threshold is 12.43 ($-\ln 4 \times 10^{-6}$) (Georgakakis et al. 2008; Laird et al. 2009; Georgakakis & Nandra 2011). To understand the effectiveness of the threshold choice, we test a few thresholds of 6, 8, 10, 12, and 14. Across the XMM-RM field, the exposure depth varies by orders of magnitude. The very-shallow part of the field has few photons and thus huge uncertainties. To calculate the logN–logS, we mask out such regions by applying a lower limit of 4×10^{15} on the soft-band Exp-ECF map, which excludes 14% of the sources and 24% of the area. We also exclude sources classified as extended or attributed to galaxy clusters (see Section 3.6). Adopting a likelihood threshold of 12, we find that the soft- and hard-band subsamples include 1557 and 564 sources, respectively.

Figure 7 displays the cumulative number counts calculated by adopting L>12 in comparison with that from the 7Ms CDFS (Luo et al. 2017) and XMM-COSMOS (Cappelluti et al. 2009), which are corrected for the different energy bands and spectral models used. The "Simple" number counts are broadly consistent with that of XMM-COSMOS within uncertainties. The CDFS counts show some deviations, which are most likely explained by sampling variance, given the very small area of the CDFS field. Having the Eddington bias corrected, the number count measured with the "Poisson" method is slightly lower than that with the "Simple" method. This correction is more significant in the hard band, which has a higher background and thus larger relative uncertainties.

The number counts calculated by adopting different thresholds are compared in the lower panels of Figure 7. When reducing the threshold, the sample is expected to contain more contamination from either spurious sources (fluctuations) or extended sources. However, on the contrary, the number counts become lower with lower thresholds, especially in the hard band where the relative uncertainties are larger. As discussed in Section 4.3, because of the large scatter of likelihoods, the PSF-fitting likelihood selected sample is incomplete with respect to the Poissonian likelihood. Although we have minimized such

incompleteness by choosing a low PSF-fitting likelihood threshold, at low likelihoods, the "Poisson" method aggravates such incompleteness: a fraction of below-flux-limit sources are considered as detectable through Poisson fluctuation but actually cannot survive the PSF-fitting preselection. Therefore, a high threshold is required to recover the logN–logS, not only in order to avoid spurious sources. With the "Poisson" method, more prominent problems to avoid are sample incompleteness and the large uncertainties at low thresholds. Above a flux limit that corresponds to an area of 0.12 deg², the L>12 and L>14 cases are highly identical with only a $\sim 1\%$ difference. With L>10, the difference of logN–logS from that of L>14 starts to be larger than the uncertainty. Therefore, we suggest adopting a threshold of 12.

5. Multiband Counterparts

5.1. Combined Legacy-unWISE Catalog

We identify multiband counterparts of the XMM-RM sources from the optical Legacy (Dey et al. 2019) and the IR unWISE (Schlafly et al. 2019) catalogs. The Legacy catalog presents g-, r-, and z-band magnitudes for each source. The unWISE catalog provides the W1 (3.4 μ m) and W2 (4.6 μ m) magnitudes, although some sources are detected in only one of the two bands. Considering that the typical XMM positional uncertainty (\sim 2", half-pixel size) is much larger than that of the optical/IR positions, we first combine the Legacy and unWISE catalogs and then match the XMM sources to the combined catalog. In order to account for the unknown systematic uncertainty of the Legacy catalog and to avoid extremely small and potentially unrealistic positional uncertainties, we add an additional systematic positional uncertainty of 0"3 in quadrature to both the Legacy and the unWISE sources. This may overestimate the positional errors of some optical sources, but it prevents failures in identifying an optical/IR match of sources caused by underestimation of positional errors in some cases, and it is small enough not to cause any problem in the X-ray

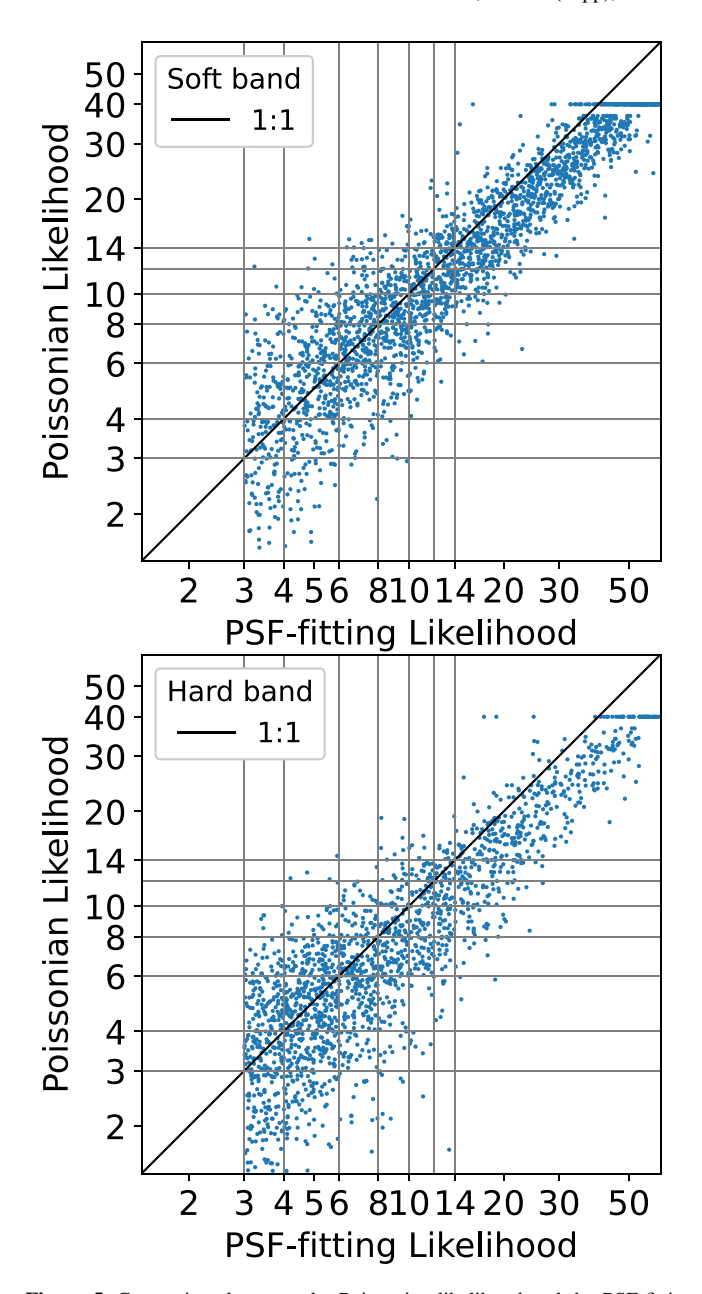


Figure 5. Comparison between the Poissonian likelihood and the PSF-fitting likelihood in the soft (top panel) and hard (bottom panel) bands.

counterpart association. As the optical positional accuracy is the best, we ran NWAY to associate the unWISE sources to the Legacy ones within 4", using the Legacy z-band magnitude prior generated through the NWAY "AUTO" method. We select the matches with $p_{\rm any} > 0.02$, which corresponds to a 5% false association rate according to a Monte Carlo test. Based on these matches, we merged all of the Legacy and unWISE sources into one catalog, including 41% LegacyunWISE pairs, 44% Legacy-only sources, and 15% unWISEonly sources. We adopt an upper limit of 24 on the IR W1 and W2 magnitudes and an upper limit of 29 on the optical g, r, and z magnitudes. The magnitudes of undetected sources are set to these upper limits. As discussed later, the simple Monte Carlo method we used leads to an overestimated false rate that is boosted high by the high density of optical sources. Because the optical/IR positional uncertainty is much better than that of

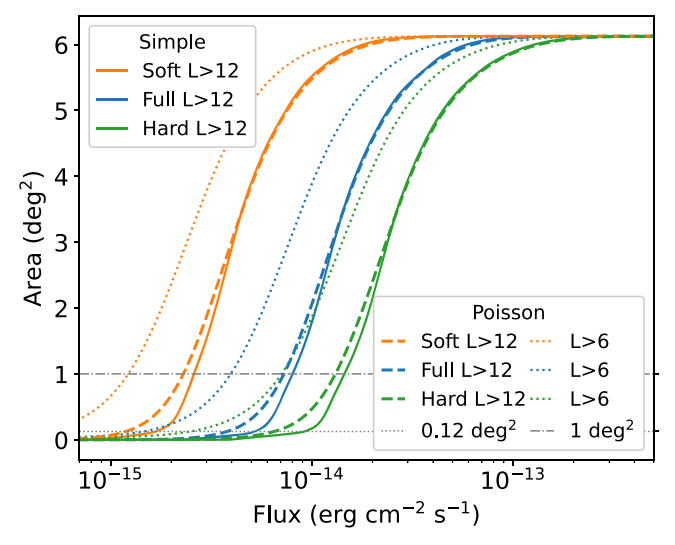


Figure 6. Sky area coverage in the three bands calculated using the "Simple" method adopting a likelihood threshold of 12 (solid lines) and using the "Poisson" method adopting likelihood thresholds of 12 (dashed lines) and 6 (dotted lines). The gray horizontal lines mark the areas of 0.12 and 1 deg².

X-ray, potential false matches and mismatches caused by abnormal positional accuracy in some rare cases cannot cause any visible problem in this work; anyway, all of the optical/IR sources are available in the stacked catalog to be picked as counterparts of X-ray sources.

5.2. Priors for X-Ray Sources

In order to efficiently identify optical/IR counterparts of the XMM-RM sources using the Bayesian method NWAY (Salvato et al. 2018), we create optical/IR color and magnitude priors on the basis of the Chandra catalogs of C-COSMOS (Marchesi et al. 2016) and Stripe 82 (LaMassa et al. 2016). Chandra sources have excellent positional accuracy (~ 0.15) and can easily be matched to the correct counterparts. We select the unWISE sources within 30" of the Chandra sources and the Legacy sources within 35" and match them as done above for the XMM-RM field. We also select the counterparts with $p_{\rm any} > 0.02$, which corresponds to a slightly higher false rate of 6% in the COSMOS field because it has a deeper Legacy coverage than the XMM-RM field. From the combined optical/ IR catalog selected within 30" of Chandra sources, we search for IR/optical counterparts using NWAY within a maximum distance of 4'' using the Legacy g band and the unWISE W1band priors generated through the NWAY "AUTO" method. We select only the reliable counterparts with $p_{\rm any} > 0.6$ (corresponding to a false rate of 5%) and $p_i > 0.6$. In order to have fluxes similar to our sample, we select only sources with soft (0.5–2 keV) fluxes >1.0 \times 10⁻¹⁵ erg cm⁻² s⁻¹; see Figure 2 for the soft flux distributions of the XMM-RM sources and the C-COSMOS and Stripe 82 Chandra sources. The selected optical/IR counterparts are compared with the other sources in the parent sample to build priors as follows.

We define an IR color in the space $W1 + W2 \sim 4(W1 - W2)$, where W1 and W2 are the unWISE magnitudes, and the factor 4 is added to stretch the distribution in the W1 - W2 direction just in order to preserve the W1 - W2 gradient during smoothing. Figure 8 displays the colors of the selected counterparts (top panel) and the other sources within 30" of the Chandra source positions (middle panel). Using the

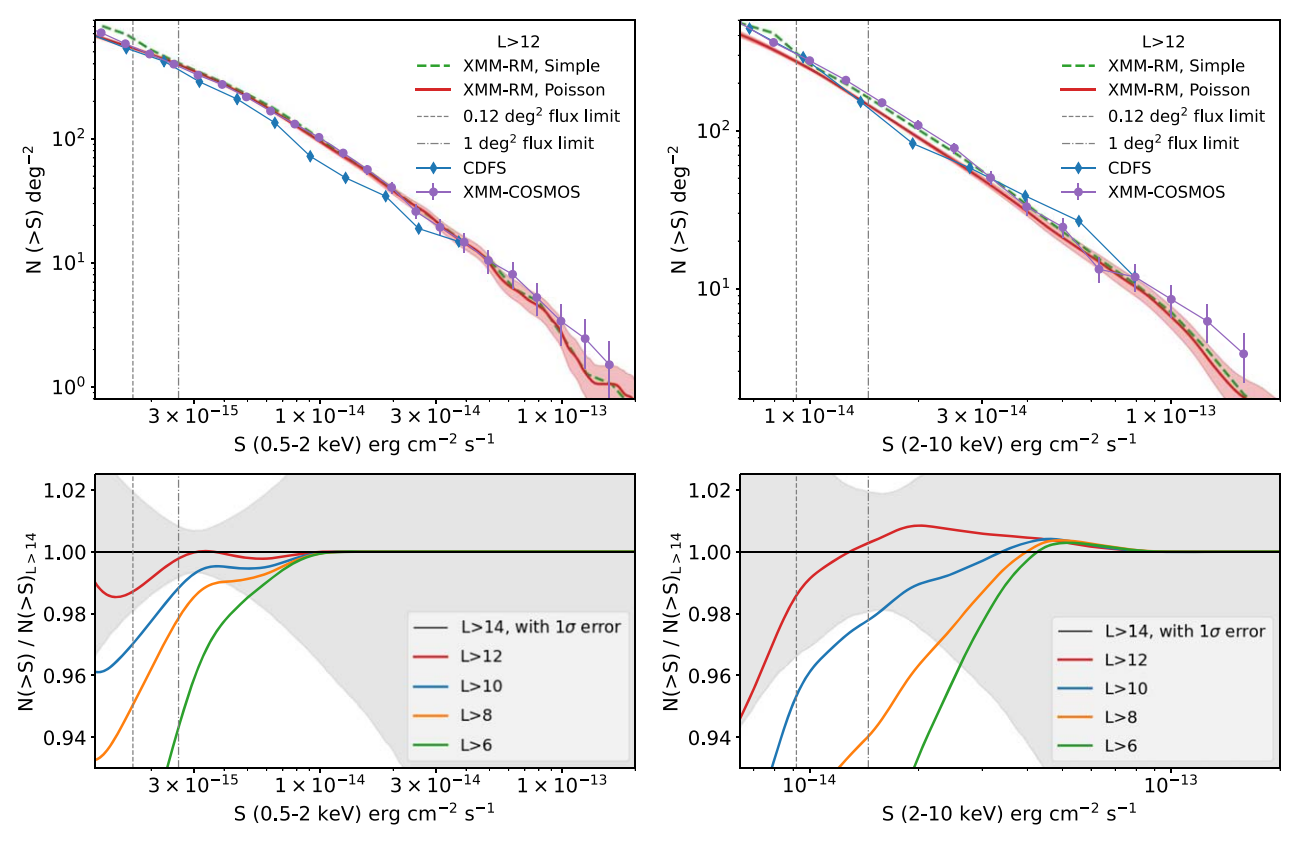


Figure 7. The upper panels display the soft (left) and hard (right) band $\log N$ - $\log S$ calculated by adopting a likelihood threshold L>12 in comparison with that of CDFS (blue diamonds, Luo et al. 2017) and XMM-COSMOS (purple points, Cappelluti et al. 2009). The green dashed line is generated using the "Simple" number counting method, and the red solid line via the "Poisson" probability distribution stacking method. The shaded region displays the 68% confidence interval calculated using the bootstrap percentile method. The lower panels compare the "Poisson" $\log N$ - $\log S$ calculated by adopting L>12 (red), L>10 (blue), L>8 (orange), and L>6 (green) with that adopting L>14 (black). In all panels, the flux limits corresponding to sky areas of 0.12 \deg^2 (XMM FOV) and 1 \deg^2 adopting L>12 are marked with gray vertical lines.

Python package "SweeplineVT" (Liu et al. 2013), Voronoi tessellation is run on these points, and the Voronoi cell area of each point is calculated. The square root of the cell area of each point is indicated as error bars in Figure 8, with a maximum cut of 1.2 applied. We pixelate the space in the ranges 22 < W1 + W2 < 44 and -7.5 < 4(W1 - W2) < 6.5 into 132×84 pixels, which guarantees a high spatial resolution of the 2D source distribution. For each point, we fill into the pixelated image a 2D Gaussian probability density function with a scale of the square root of its cell area (error bars in Figure 8). Limited by the sample size, the distribution is not sufficiently smoothed across the space. Thus we adopt a further Gaussian smoothing using a scale of two pixels. The ratio between the smoothed distributions (bottom panel of Figure 8) is used as the prior for counterparts of X-ray sources.

As shown in Figure 8, we manually draw a horizontal line at 4(W1 - W2) = -3 and a line with a slope of 4 (black lines), and we consider the region below these lines as a forbidden region by setting the probability of this region to the minimum value in the prior distribution. We also add three special pixels in the prior image, which are marked with red, yellow, and cyan circles in Figure 8, in order to store the values for three special cases: the unWISE sources detected only in the W1 band (red) and only in the W2 band (yellow) and the unWISE-undetected sources (cyan). Taking these three special categories into account, this magnitude–color prior covers almost the entire parameter space. The uncovered region (blue region in Figure 8) contains barely any sources.

Figure 9 displays the normalized Legacy *g*-, *r*-, and *z*-band magnitude distributions of the reliable counterparts of Chandra sources (blue) and the other Legacy sources (orange). These magnitude distributions can also be used as priors for selecting counterparts of X-ray sources. We do not create an optical color prior as done above for the unWISE color, because it is likely to introduce a bias against type II AGNs.

5.3. Optical/IR Counterparts of XMM-RM Sources

Having established the prior based on the Chandra data, we turn back to the XMM-RM field. From the Legacy-unWISE combined catalog, we select the sources within 30" of all the XMM sources as the candidate sample, whose total area is 0.74 deg². We run NWAY with a completeness prior of 0.7 and a maximum distance of 15", using a series of prior choices as described below. As a Monte Carlo test, we redistribute the XMM-RM sources randomly in the XMM-RM footprint. We maintain a minimum separation of 10" among the random positions, but we do not purposely keep away from the position of real sources. The test is repeated five times to improve the statistics. The completeness and false rate at any $p_{\rm any}$ threshold based on the different prior choices are compared in Figure 10. Achieving a higher completeness and a lower false rate at the same time indicates a more efficient identification. First, we run without any additional prior, for example, based on only positions and their uncertainties. Then we use the g-band prior created above using Chandra sources. This improves the identification

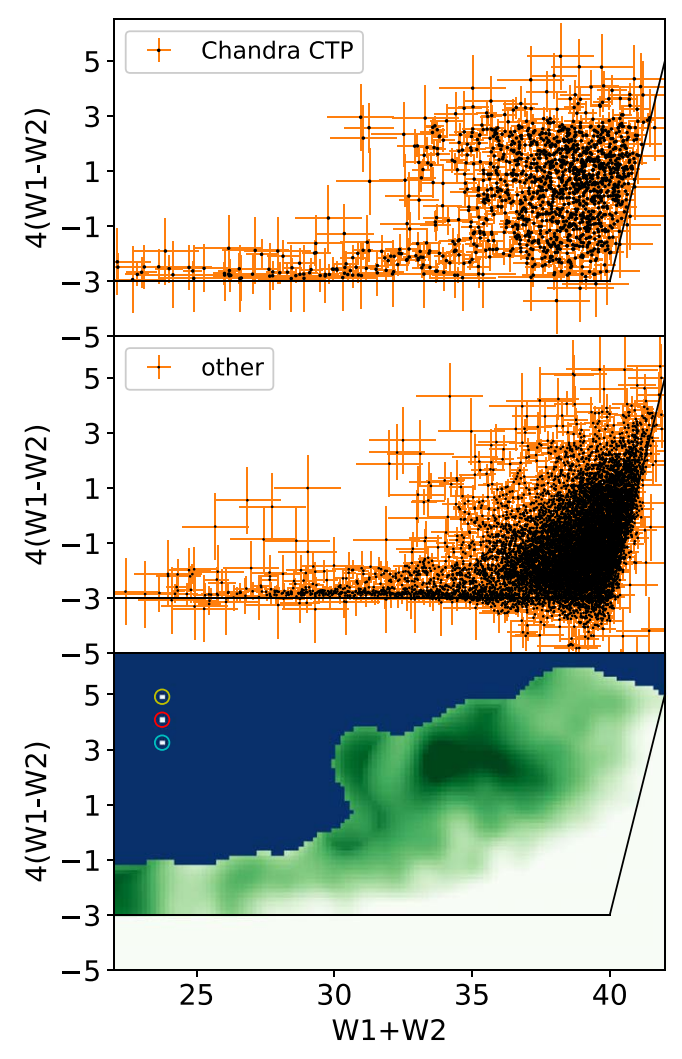


Figure 8. The top and middle panels display the distributions of the unWISE counterparts of Chandra sources and the other unWISE sources within 30" of Chandra sources. The error bar corresponds to the square root of the Voronoi cell area of each point. The bottom panel presents the color-coded prior in terms of the ratio between the smoothed distributions of the top and middle panels, from low to high value in green color from light to dark. The blue region is not used. The three special pixels marked with red, yellow, and cyan circles correspond to unWISE sources detected only in W1, only in W2, and unWISE-undetected sources, respectively. The two axes have the same scaling from data to plotting units.

efficiency slightly. Replacing the g prior with the unWISE prior (W), we find a significant improvement. Adopting the W prior, we then tried adding (1) the g prior, (2) the g and r priors, and (3) the g, r, and g priors. We find that the more optical priors we add, the less efficient the identification is. This is because the magnitudes in different bands are correlated, so adding them does not introduce much additional independent information. On the other hand, adding further unnecessary priors pushes up the g-any values of bright sources that are occasionally matched to random positions. Therefore, we present the NWAY results using only the unWISE prior.

One X-ray source can have multiple SDSS/unWISE counterparts identified by NWAY. For the sake of completeness, all of the counterparts from NWAY using the unWISE prior are provided along with this paper (see the Appendix).

As shown in Figure 10, selecting the best NWAY counterparts with p_{any} above 0.78, 0.63, and 0.36 leads to a completeness

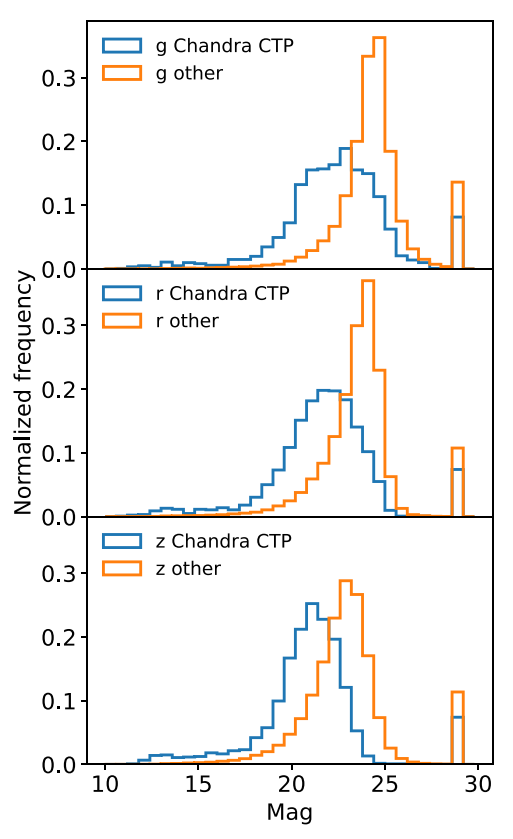


Figure 9. Normalized *g*-, *r*-, and *z*-band magnitude distributions of the reliable counterparts of Chandra sources (blue) and the other Legacy sources (orange).

of 63%, 74%, and 84% with corresponding false-counterpart identification rates of 5%, 10%, and 20%, respectively. Here the false rate is defined as the probability of finding any optical/IR counterpart at a random position. A high false rate measured by the Monte Carlo test is partially caused by the large XMM positional uncertainty. More importantly, it is because the Legacy and unWISE surveys are both very deep and combining them results in a high density of sources. We remark that such a false rate is much higher than the genuine probability of one counterpart being false, because in the highly crowded optical/ IR catalog, many sources are not potential counterparts of X-ray sources. As shown in Figure 11, adopting $p_{\text{anv}} > 0.36$, we find that the best counterparts of real sources and of random positions are significantly different in magnitudes and colors. The difference is large even if adopting a strict threshold of $p_{\rm any} > 0.78$. The counterparts of random positions tend to be fainter and more likely undetectable in some bands. Therefore, we recommend allowing a relatively higher false rate for these counterparts, for example, 10% or 20%, rather than 5% or 1%.

5.4. Astrometric Accuracy

To test if an additional systematic positional uncertainty is present, we compare the distribution of X-ray-optical/IR source separation with the Rayleigh distribution in Figure 12. This method relies on the fact that the distribution of the ratio $x = \Delta r/\sigma_{\rm tot}$, where Δr is the separation between the X-ray source and its optical/IR counterpart and $\sigma_{\rm tot}$ is the total one-dimensional positional error $\sqrt{\sigma_X^2/2 + \sigma_{\rm opt/IR}^2/2}$, should follow the Rayleigh distribution $f(x) = x \exp(-x^2/2)$, as long as $\sigma_{\rm tot}$ is an accurate estimate of the true positional error (Watson et al. 2009; Rosen et al. 2016; Pineau et al. 2017).

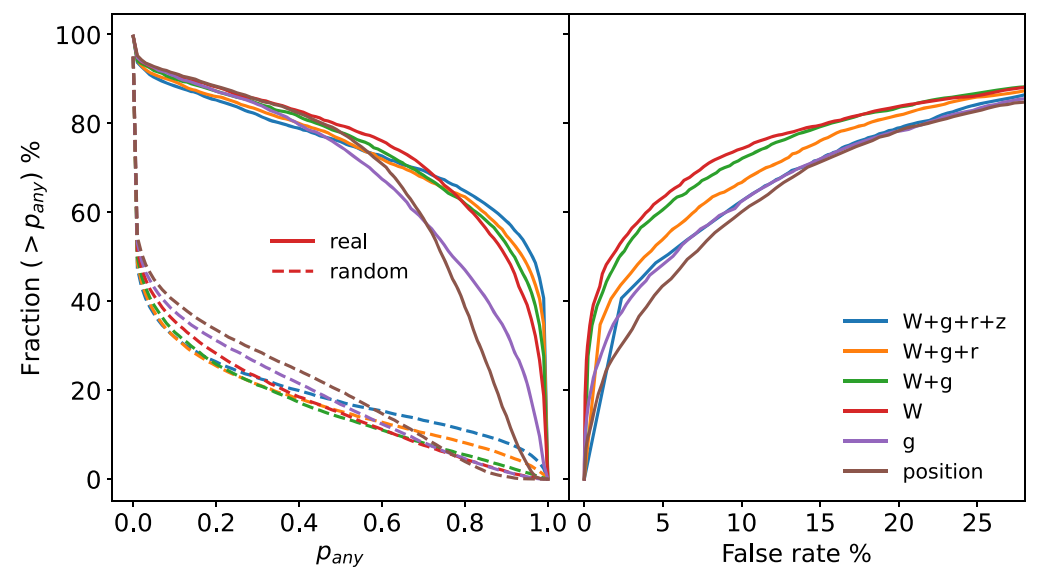


Figure 10. The left panel displays the cumulative distributions of p_{any} of real sources (solid lines) and of random positions (dashed lines), which represent the completeness and false rate of the counterpart selection. The right panel shows the completeness as a function of false rate with a varying p_{any} threshold. The cases of adopted priors include no additional prior (position only), g-band magnitude prior (g), unWISE prior (W), and unWISE prior plus one or multiple magnitude priors (W + g, W + g + r, W + g + r + z).

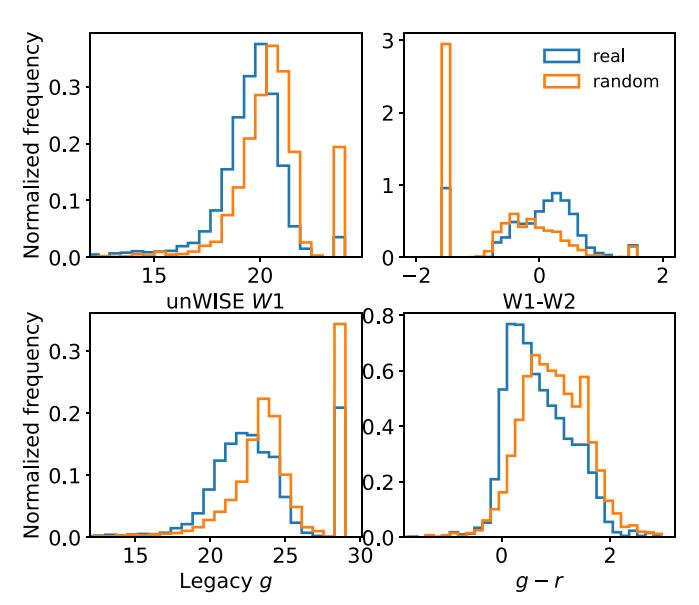


Figure 11. Comparison of magnitudes (unWISE W1, Legacy g) and colors (W1-W2, g-r) of the best counterparts of the real sources (blue) and random positions (orange) with $p_{\rm any}>0.36$. Legacy-undetected sources are set as g=29; unWISE-undetected sources are set as W1=24. unWISE sources detected in only one of the W1 and W2 bands are plotted as W1-W2=1.5 or g=1.5

Adopting a $p_{\rm any}$ threshold that corresponds to a 20% false rate (blue line), we have an excess tail above the Rayleigh distribution at high x. By adopting a higher threshold that corresponds to a 5% false rate (red line), we find the distribution fits the Rayleigh distribution much better. These results are broadly consistent with that found by Rosen et al. (2016) for the 3XMM catalog; see a more detailed discussion therein. The tail excess can be caused by spurious matches or underestimation of positional uncertainties in some cases probably at high off-axis angles. For the majority of the catalog, the positional uncertainties are accurate and need no additional correction.

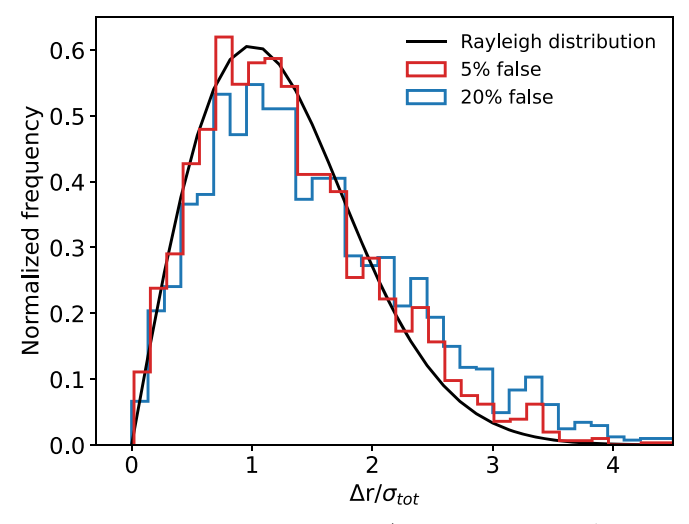


Figure 12. Distributions of X-ray to optical/IR position separation Δr in units of total one-dimensional positional uncertainty $\sigma_{\rm tot} = \sqrt{\sigma_{\rm x}^2/2 + \sigma_{\rm opt/IR}^2/2}$. The red and blue lines indicate selections of $p_{\rm any} > 0.78$ and $p_{\rm any} > 0.36$, respectively. The black line is the Rayleigh distribution.

5.5. SDSS Spectra and Best Counterparts

We search for SDSS spectra of the optical/IR counterparts from the DR16 catalog (York et al. 2000) through a positional match within a radius of 1" (BOSS fiber radius) and find 1206 SDSS spectra for 1141 X-ray sources, including 847 AGNs, 312 galaxies, and 47 stars. A total of 71% of the AGNs (603) are in the SDSS-RM quasar catalog (Shen et al. 2019). Five sources have SDSS spectroscopic redshifts >5. Since such high redshifts from the SDSS spectroscopic pipeline are often unreliable, we visually examined these spectra. Better fits with smaller redshifts are found for two of them (both $z \approx 2$). We replace their SDSS redshifts with the manually fitted ones. For the other three, the spectra are too noisy to provide robust redshift measurements. We exclude them from further analysis by multiplying their SDSS redshifts by -1.

NWAY calculates p_i on the basis of priors that are generated considering all of the X-ray sources as a population with similar magnitude and color distributions, regardless of source types. Such priors are a good choice for the majority of the sample, but not necessarily appropriate for each individual source. Specifically, the priors favor optical/IR sources that appear brighter. Although AGNs are more likely X-ray emitters than stars, stars that are often brighter in optical/IR will be assigned higher probabilities according to the priors. Therefore, rather than simply selecting the best counterpart as the one with $match_flag == 1$, which means the highest p_i in NWAY, we select the best counterpart for each X-ray source while taking into account the SDSS spectra.

In 915 cases, the SDSS spectroscopic objects are identified as the best ($match_flag == 1$) counterparts of X-ray sources. In the other 226 cases, a better counterpart with a higher p_i than the SDSS spectroscopic object is found in the unWISE-Legacy catalog, which is deeper than the SDSS catalog. We note that in 17 such cases, the position-based posterior matching probability (dist_post) of the SDSS spectroscopically confirmed AGNs is even higher than or at least approximately equal to that of the best unWISE-Legacy counterpart, indicating such SDSS AGNs have relatively lower p_i than other unWISE-Legacy sources only because of the priors adopted. However, it should be considered as a strong additional prior that AGNs tend to be X-ray emitters. Therefore, we select the SDSS objects as the best counterparts of these 17 sources, and in other cases, we select the one with $match_flag == 1$.

Among the selected best counterparts, there are 932 SDSS spectroscopic objects. For the ones in SDSS-RM, we adopt the redshift and class (AGN) from SDSS-RM (Shen et al. 2019), which were examined carefully, instead of the pipeline results of the SDSS DR16 catalog. We also visually inspect the non-AGN SDSS spectra and find 21 sources have both a high X-ray luminosity ($\log L_{\rm X} > 42.5$ erg s⁻¹) and a type II AGN-like spectrum (e.g., with a strong, narrow [OIII] emission line). Their classes are manually changed to AGN. Eventually, there are 831 AGNs (594 SDSS-RM quasars), 96 galaxies, and five stars.

Figure 13 displays the unWISE W1-W2 color, the W1 AB magnitude, and the SDSS g-r color of the best counterparts as a function of the soft-band X-ray fluxes. The spectroscopically confirmed AGNs have relatively bluer optical color and redder IR color, and almost all of them lie above the empirical line suggested by Salvato et al. (2018) to separate AGNs from normal galaxies and stars ($W1_{\text{Vega}} = -1.625 \times \text{logFlux}_{0.5-2\text{keV}} - 8.8$).

For the AGNs and galaxies with SDSS spectroscopic redshifts, we calculate the rest-frame 2–10 keV luminosities assuming a power law with a photon index of 1.7 and Galactic absorption (HI4PI Collaboration et al. 2016). In general, the soft-band flux is preferentially used to calculate the luminosity. However, at z < 1, we choose the hard band to avoid a large k-correction as long as the hard-band relative flux uncertainty (ratio of flux error to flux value) $\Delta f_{\rm Hard}$ is lower than 0.7 or $\Delta f_{\rm Soft} + 0.2$, where $\Delta f_{\rm Soft}$ is that in the soft band. The luminosity–redshift distribution of these sources is shown in Figure 14.

5.6. Undetected SDSS-RM Quasars

Among the 756 SDSS-RM quasars (90% of the whole sample) covered by the XMM exposures, 594 (78%) are identified as the best counterparts of X-ray sources. For the other 162 quasars in the XMM FOV, it is not necessarily true that there are no X-ray

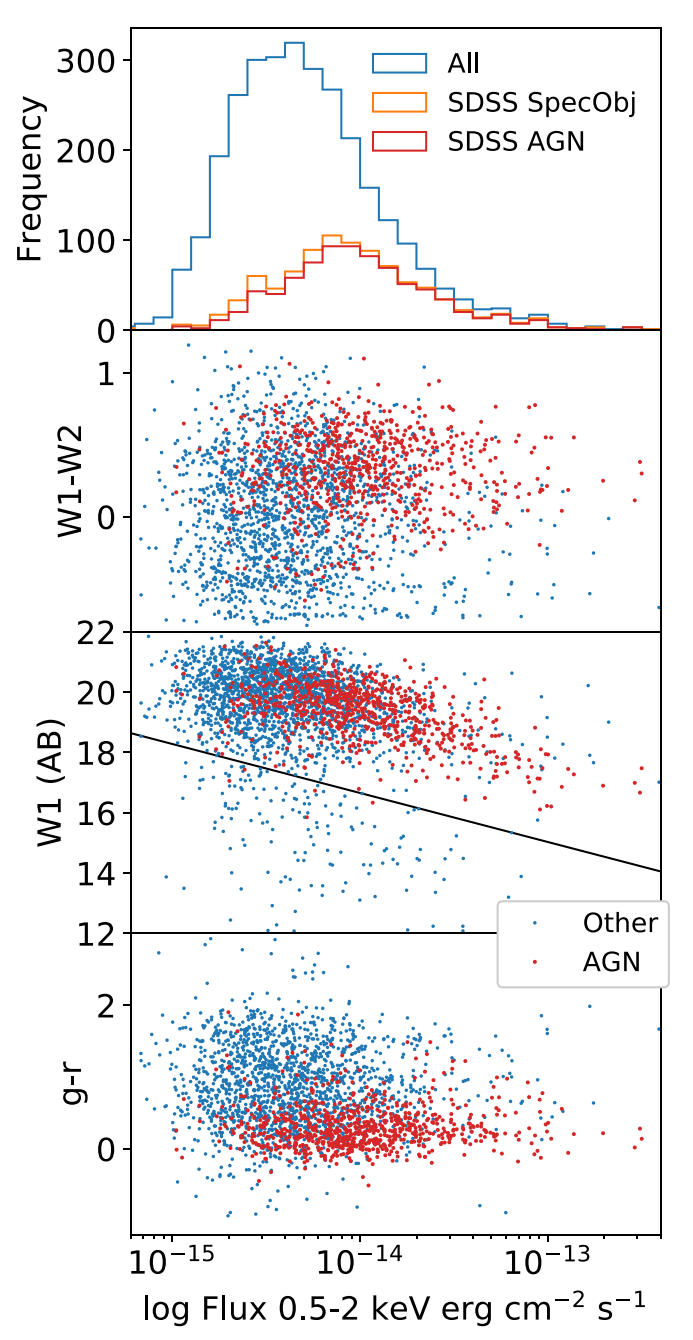


Figure 13. The top panel displays the X-ray flux distributions of all sources (blue), the SDSS spectroscopically observed ones (orange), and the spectroscopically confirmed AGNs (red). The other panels display the unWISE W1-W2 color (top), the W1 AB magnitude (middle), and the SDSS g-r color (bottom) of the best counterparts as a function of the X-ray fluxes. A source is plotted in red if classified as an AGN. The black line is the empirical line from Salvato et al. (2018) to separate AGNs from galaxies and stars.

signals at their positions. For 12 of them, X-ray sources are detected within 16" (the aperture radius used in this work). Nine out of the 12 are identified as possible counterparts of X-ray sources but not the best ones. We put the RMID of these nine quasars in the X-ray catalog, adding 1000 to the RMID to separate them from the best counterparts. Considering the uncertainties and complexities in both the X-ray positional accuracy and the multiband counterpart association, we cannot rule out the possibility that they might be the true counterparts of the X-ray sources.

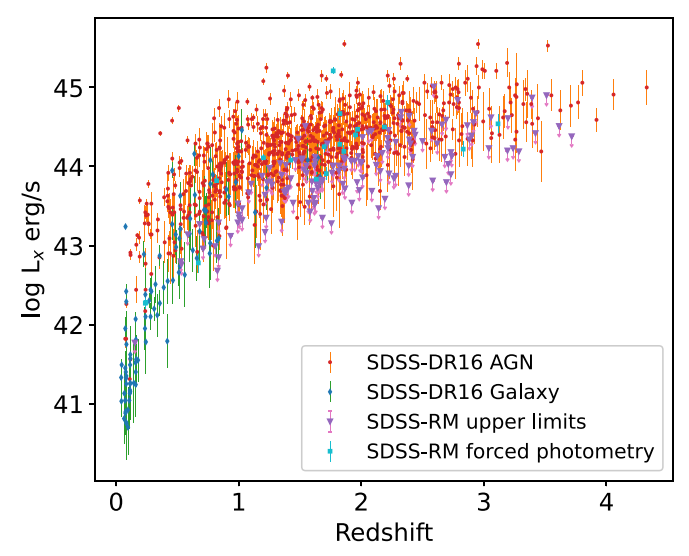


Figure 14. Distribution of the rest-frame 2–10 keV luminosity and SDSS spectroscopic redshifts. The red circular points indicate spectroscopically confirmed AGNs; the blue diamonds indicate galaxies; the cyan squares are measured through forced photometry at the positions of SDSS-RM quasars; and the purple triangles are upper limits of X-ray-undetected SDSS-RM quasars.

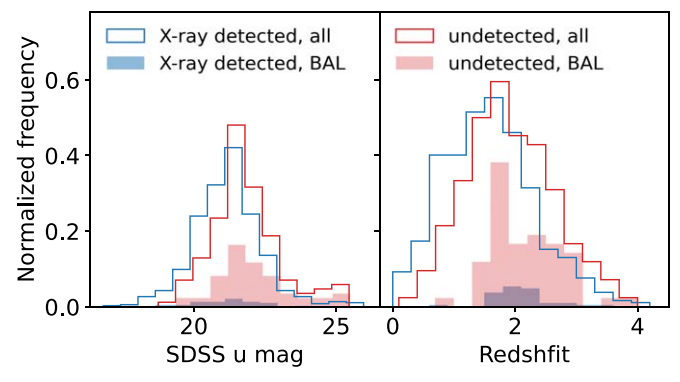


Figure 15. Normalized u magnitude (left) and redshift (right) distributions of the X-ray-detected (blue) and X-ray-undetected (red) SDSS-RM quasars. The shaded region shows the fraction of BAL quasars in each sample.

As described in Section 4.3, we perform forced photometry at the positions of all 162 quasars within a circle of radius 16", and we calculate aperture Poissonian detection likelihoods for them. We find 22 quasars with a likelihood >7 in any of the three bands and consider them as X-ray detected, leaving 140 quasars that are truly X-ray undetectable. The source net counts and upper limits are converted to fluxes using the EEF and Exp-ECF maps (Figure 4) and to luminosities as described in Section 5.5. The luminosities and upper limits are plotted in Figure 14. These forced-photometry results are also available with this paper as a supplementary catalog (see the Appendix).

Figure 15 compares the X-ray-detected SDSS-RM quasars, either as the best counterparts of the sources in the main XMM-RM catalog or through the Poissonian likelihood selection based on forced photometry, with the X-ray-undetected ones. These undetected quasars are relatively fainter (with a median u magnitude of 21.7) and have relatively higher redshifts (median redshift 1.8) compared with the detected ones (median u 21.2, median z 1.5). Meanwhile, the fraction of broad-absorption-line (BAL) quasars, which are generally known to be X-ray weak (e.g., Gallagher et al. 2006; Gibson et al. 2009), is much higher in

the X-ray-undetected sample (37%) than in the X-ray-detected sample (5%). Excluding the z < 1.6 part, where BAL identification is difficult because the broad CIV line is not well covered by the SDSS wavelength range, we find that the fraction of BAL quasars in the X-ray-undetected sample is 50%.

6. Discussion and Conclusion

6.1. The XMM-RM Catalog

With more than 40 XMM-Newton observations that cover 90% of the SDSS-RM field to an exposure depth of $\sim\!15$ ks, the XMM-RM project adds to the comprehensive multiwavelength coverage of the SDSS-RM quasar sample (Shen et al. 2019). This paper presents the XMM-RM X-ray catalog and the optical/IR counterparts of the sources. More detailed analyses of X-ray spectra, multiband colors, and spectral energy distributions based on this catalog will be presented in a subsequent paper.

We perform elaborate processing of the XMM data with the aim of optimizing the detection sensitivities for faint point sources, and we perform source detection using a simultaneous PSF-fitting technique that adopts the correct PSF model at any position of a camera during each individual observation. We choose a relatively low PSF-fitting likelihood threshold of L>3, which corresponds to a spurious fraction of $\sim 5\%$, and compile a catalog of 3553 sources. We also calculate a Poissonian detection likelihood for each source and perform further sample refinement on the basis of this likelihood. Subsamples selected in this manner show a logN–logS distribution consistent with previous X-ray surveys.

We combine the optical Legacy and the IR unWISE catalogs in the SDSS-RM field and search for counterparts of the X-ray sources in the combined catalog using the Bayesian method "NWAY." We create a two-dimensional unWISE magnitude and color prior using Chandra catalogs, which have excellent positional accuracy. This prior is effective in improving the efficiency of counterpart identification. Adopting $p_{\rm any}>0.36$ and $p_{\rm any}>0.63$ produces subsamples of optical/IR counterparts of 2987 (84%) and 2648 (74%) sources, respectively. According to Monte Carlo tests, the false association rates of these subsamples are lower than 20% and 10%, respectively.

We find SDSS DR16 spectra for 932 of our X-ray sources: 831 of them (89%) are classified as AGNs, and 594 (71%) of these AGNs are in the SDSS-RM quasar catalog. For the SDSS-RM quasars that are not associated with any X-ray sources, we calculate upper limits on their X-ray fluxes.

6.2. X-Ray Catalogs: Depth vs. Purity

It has been common practice for X-ray surveys to provide highpurity catalogs with spurious fractions as low as 1% (e.g., Cappelluti et al. 2009; Laird et al. 2009; Georgakakis & Nandra 2011; Nandra et al. 2015; Civano et al. 2016; Chen et al. 2018), prioritizing sample purity over survey depth. In this work, we recommend a new approach dispensing with it, in consideration of the fact that these two figures of merit are preferred differently in different situations. In the case of X-ray population studies, which rely on a well-defined X-ray selection function, it is essential to guarantee the sample purity through a high selection threshold, whereas a large number of sources at the faint end are expendable. In the case of studying multiband properties, especially when some sources detected in other bands are of special interest, it can be advantageous to lower the detection threshold to yield as many candidate X-ray sources as possible, even if many are

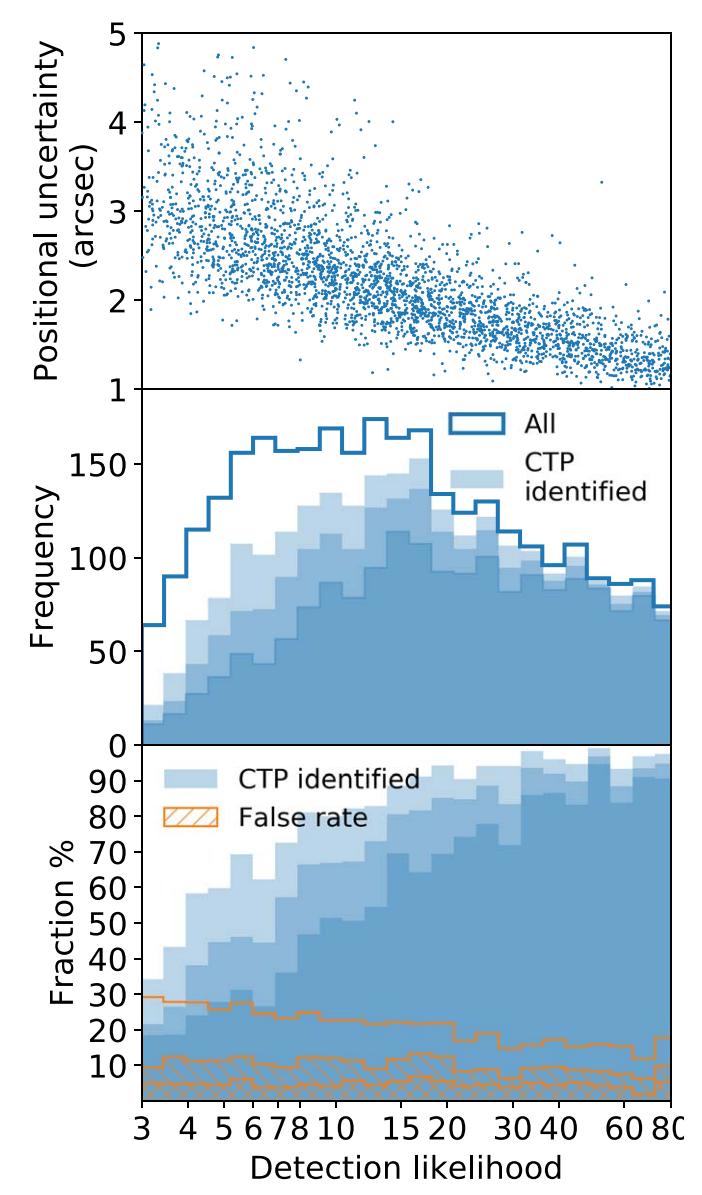


Figure 16. The top panel is the scatter plot of the total positional uncertainty and PSF-fitting likelihood of the XMM-RM sources. The middle panel presents the likelihood distributions of all of the XMM-RM sources (empty) and of the ones having counterparts (filled). The three levels of blue color depth of the filled histograms correspond to the $p_{\rm any}$ thresholds of 0.36, 0.63, and 0.78, from light to dark; the corresponding fractions in each bin are displayed in the bottom panel. The orange histograms are the fractions of the randomly distributed sources with counterparts identified; the three levels of $p_{\rm any}$ thresholds 0.36, 0.63, and 0.78 are indicated with no filling, linear hatching, and cross-hatching, respectively.

spurious. Therefore, we recommend presenting a large master catalog by adopting a relatively low detection likelihood. Population analysis (e.g., logN–logS) of X-ray sources can be carried out by applying a post hoc selection on the Poissonian detection likelihood, which gives rise to a high-purity subsample with a well-defined selection function. Such an approach will also be adopted in the ongoing eROSITA X-ray surveys (Merloni et al. 2012; T. Liu et al. 2020, in preparation).

Oriented toward the best completeness (or detection sensitivity), we not only make every effort during the data reduction to increase the S/N but also merge the catalogs detected in three bands, which yields a higher completeness at the expense of a poorly defined X-ray selection function.

Choosing a low detection likelihood threshold of L > 3, we find that the XMM-RM catalog contains a large number of lowlikelihood sources (one-third at L < 10; see the middle panel of Figure 16). As discussed in Section 4.4, the low detection likelihood is helpful as it improves the completeness of the Poissonian-likelihood selected subsample. We also show the value of including these low-likelihood sources by identifying their optical/IR counterparts. As shown in Figure 16, the counterpart identification completeness drops at low detection likelihoods. It is caused not only by higher fractions of spurious sources at low likelihoods, but also by the fact that the lowlikelihood sources (1) have larger positional uncertainties (Figure 16 top panel) and thus lower posterior probabilities for real counterparts; (2) have their positions more easily affected by unaccounted factors, such as CCD gaps and nearby undetectable sources; and (3) have relatively lower fluxes in both X-ray and optical/IR bands and might drop out of the optical/IR detection limits. The fraction of random-position counterparts (false rate) increases slightly with decreasing likelihood (Figure 16 bottom panel), as a result of the increasing positional uncertainty. Even when taking the increasing false rate into account, we have a significant fraction of sources at low likelihoods with reliable counterparts identified, at least above a likelihood of 4, not to mention that the false rate is overestimated (Section 5.3). Considering the existence of multiband counterparts as an additional prior, the posterior probabilities of these sources being real should be high. It would be a loss to exclude such sources, which are numerous, from the master catalog.

W.N.B. acknowledges support from NASA grant 80NSSC19K0961 and NASA ADAP grant 80NSSC18K0878. Y.S. acknowledges support from an Alfred P. Sloan Research Fellowship and NSF grant AST-1715579. L.C.H. was supported by the National Science Foundation of China (11721303, 11991052) and the National Key R&D Program of China (2016YFA0400702).

Appendix XMM-RM Catalogs

In addition to the primary XMM-RM catalog, we provide a supplementary catalog presenting the forced aperture photometry results of the X-ray-undetected SDSS-RM quasars and the full NWAY output table matching the XMM-RM catalog to the combined Legacy—unWISE catalog when adopting the unWISE magnitude—color prior, which contains all of the possible counterparts of the X-ray sources. They are available in the data.tar.gz package and can also be obtained at https://www.mpe.mpg.de/XraySurveys/XMM-RM/.

The columns of the primary XMM-RM catalog are described in three groups in Appendices A.1, A.2, and A.3. In all of the catalogs, values are set to –99 if not applicable.

A.1. Unique Source Parameters

The following columns present basic information for each X-ray source.

ID: unique X-ray ID in the XMM-RM catalog

RA,DEC: X-ray coordinates (J2000) in degrees

RADEC_ERR: X-ray positional uncertainty from PSF fitting (combined RADEC error) in arcseconds

SYSERRCC: additional systematic positional uncertainty that needs to be added to RADEC_ERR in quadrature to measure the total positional uncertainty

(Continued)

DetBand: The detection band is the band (F, S, H) that has the highest detection likelihood and in which the source position, DET_ML, and extent are measured.

DET_ML: detection likelihood from PSF fitting using emldetect

EXT,EXT_ERR: source extent and uncertainty (beta-model core radius) in pixels (4" per pixel)

EXT_ML: source extent likelihood, i.e., the likelihood difference between a beta-model fit and a PSF model fit

NHI: Galactic column density at the source position in cm⁻² from HI4PI (HI4PI Collaboration et al. 2016)

NNDist: distance to nearest neighbor in arcseconds, set to 120" if having no neighbor within 120"

RMID: SDSS-RM catalog ID. RMID > 1000 means the RMID is added by 1000 and this quasar is not identified as the best counterpart of the X-ray source.

SpecObjID: SDSS DR16 spectroscopic object ID

SDSS_Cluster: ID in the Wen et al. (2012) SDSS cluster catalog

z,zErr: SDSS spectroscopic redshift, modified if necessary (Section 5.5)

Class: SDSS spectroscopic classification (1: AGN; 2: galaxy; 3: star), modified if necessary (Section 5.5)

Lx,LxErr: rest-frame 2–10 keV luminosity (erg s⁻¹) and 1σ uncertainty propagated from the flux uncertainty

A.2. Parameters for Each Band

The following columns present the source properties measured in the full (F), soft (S), and hard (H) bands.

SCTS_[FSH],SCTS_ERR_[FSH]: source counts and error from PSF fitting using emldetect

DET_ML_[FSH]: detection likelihood from PSF fitting using emldetect BG_MAP_[FSH]: background at source location in counts per pixel RATE_[FSH],RATE_ERR_[FSH]: source count rate and error in counts $\rm s^{-1}$ from emldetect

RA_[FSH],DEC_[FSH]: coordinates (J2000) in degrees

RADEC_ERR_[FSH]: positional uncertainty from PSF fitting (combined RADEC error) in arcseconds

EXP_[FSH]: sum of the vignetted exposure (seconds) of the three EPIC cameras

Flux_[FSH],FluxErr_[FSH]: flux and error (10⁻¹⁴ erg cm⁻² s⁻¹) in the 0.5-10 (F), 0.5-2 (S), and 2-10 (H) keV bands. In the primary catalog, they are measured from the PSF-fitting count rate; in the supplementary forced-photometry catalog, they are measured from the aperture count rate.

NetCtsA_[FSH]: background-subtracted aperture source counts measured within 16" using eregionanalyse

TotCtsA_[FSH]: total counts within 16" from eregionanalyse. TotCtsA-NetCtsA is the aperture background counts.

RateUpperA_[FSH]: 2σ count rate upper limit on the background-subtracted aperture source count rate

 $\ensuremath{\mathsf{EEF}}\xspace_{-}\xspace[FSH]\xspace{-1.5ex}$ enclosed energy fraction of 16'' at the source location on the $\ensuremath{\mathsf{EEF}}\xspace$ map

APLike_[FSH]: aperture Poissonian likelihood, calculated adopting a maximum of 40

ExpECF_[FSH]: value at the source location on the Exp-ECF map, which is used to convert the net source counts in the 0.5–7.5 (F), 0.5–2 (S), and 2–7.5 (H) keV bands to fluxes in the 0.5–10 (F), 0.5–2 (S), and 2–10 (H) bands

A.3. Parameters of Counterparts

The following columns present NWAY association information of the best optical/IR counterpart from the combined Legacy–unWISE catalog. Please refer to Salvato et al. (2018) for more detailed descriptions.

UW_RA,UW_DEC: unWISE source coordinates (J2000) in degrees UW ID: unWISE source ID

UW_W1_AB,UW_W1ERR: unWISE W1 AB magnitude and error

(Continued)

UW_W2_AB,UW_W2ERR: unWISE W2 AB magnitude and error LS_RA,LS_DEC: Legacy source coordinates (J2000) in degrees

LS_BRICKNAME: Legacy brick name

LS_BRICKID: Legacy brick ID LS_OBJID: Legacy object ID

LS_Mag_[rgz]: Legacy AB magnitude in the r, g, and z bands

 p_{any} : the probability that any of the associations is the correct one

pi: relative probability of the match

match_flag: 1 for the most probable match, 2 for less probable matches with $p_i/p_i^{\text{best}} > 0.5$

Separation: separation between the pair of sources in arcseconds

dist_bayesfactor: logarithm of ratio between prior and posterior from distance matching

dist_post: distance posterior probability comparing this association versus no association

 p_{single} : same as dist_post, but weighted by the unWISE magnitude-color prior CellInd: index of the $W1+W2\sim 4(W1-W2)$ cell in which the source is located (Section 5.2)

bias_UWLS_CellInd: probability weighting introduced by the unWISE color prior

A.4. Exclusive Columns of the SDSS-RM Forced-photometry Catalog

Most of the columns of the supplementary catalog are the same as the primary catalog (Appendices A.1, A.2), except for a few:

RA,DEC: SDSS-RM quasar coordinates (J2000) in degrees

FluxUpper_[FSH]: 2σ flux upper limit measured from RateUpperA

LxUpper: 2σ upper limit of rest-frame 2–10 keV luminosity (erg s⁻¹) measured from RateUpperA

A.5. Exclusive Columns of the NWAY Output Table

Most of the columns of the NWAY output table are already described in Appendix A.3, except for the following:

X_ID,X_RA,X_DEC,X_POSERR: the X-ray ID, coordinates, and total positional uncertainties (Appendix A.1)

UWLS_RA,UWLS_DEC,UWLS_POSERR: the coordinates and positional uncertainties of the combined Legacy—unWISE catalog, adopting that of the Legacy sources when available and the unWISE sources in the other cases

ORCID iDs

Mara Salvato https://orcid.org/0000-0001-7116-9303
Johannes Buchner https://orcid.org/0000-0003-0426-6634
Yue Shen https://orcid.org/0000-0003-1659-7035
Kirpal Nandra https://orcid.org/0000-0002-7150-9192
Luis C. Ho https://orcid.org/0000-0001-6947-5846

References

Blanton, M. R., Bershady, M. A., Abolfathi, B., et al. 2017, AJ, 154, 28 Cappelluti, N., Brusa, M., Hasinger, G., et al. 2009, A&A, 497, 635 Cash, W. 1979, ApJ, 228, 939 Chen, C. T. J., Brandt, W. N., Luo, B., et al. 2018, MNRAS, 478, 2132

Civano, F., Marchesi, S., Comastri, A., et al. 2016, ApJ, 819, 62

Davis, M., Guhathakurta, P., Konidaris, N. P., et al. 2007, ApJL, 660, L1

```
Dawson, K. S., Schlegel, D. J., Ahn, C. P., et al. 2013, AJ, 145, 10
Dey, A., Schlegel, D. J., Lang, D., et al. 2019, AJ, 157, 168
Eisenstein, D. J., Weinberg, D. H., Agol, E., et al. 2011, AJ, 142, 72
Gabriel, C., Denby, M., Fyfe, D. J., et al. 2004, in ASP Conf. Ser., 314,
   Astronomical Data Analysis Software and Systems (ADASS) XIII, ed.
   F. Ochsenbein, M. G. Allen, & D. Egret (San Francisco, CA: ASP), 759
Gallagher, S. C., Brandt, W. N., Chartas, G., et al. 2006, ApJ, 644, 709
Georgakakis, A., & Nandra, K. 2011, MNRAS, 414, 992
Georgakakis, A., Nandra, K., Laird, E. S., Aird, J., & Trichas, M. 2008,
      RAS, 388, 1205
Gezari, S., Martin, D. C., Forster, K., et al. 2013, ApJ, 766, 60
Gibson, R. R., Jiang, L., Brandt, W. N., et al. 2009, ApJ, 692, 758
Goulding, A. D., Forman, W. R., Hickox, R. C., et al. 2012, ApJS, 202, 6
HI4PI Collaboration, Ben Bekhti, N., Flöer, L., et al. 2016, A&A, 594, A116
Kaiser, N., Burgett, W., Chambers, K., et al. 2010, Proc. SPIE, 7733, 77330E
Komatsu, E., Smith, K. M., Dunkley, J., et al. 2011, ApJS, 192, 18
Laird, E. S., Nandra, K., Georgakakis, A., et al. 2009, ApJS, 180, 102
LaMassa, S. M., Urry, C. M., Cappelluti, N., et al. 2016, ApJ, 817, 172
Lang, D., Hogg, D. W., & Schlegel, D. J. 2016, AJ, 151, 36
Liu, T., Tozzi, P., Tundo, E., et al. 2013, A&A, 549, A143
```

```
Luo, B., Brandt, W. N., Xue, Y. Q., et al. 2017, ApJS, 228, 2
Marchesi, S., Lanzuisi, G., Civano, F., et al. 2016, ApJ, 830, 100
Merloni, A., Predehl, P., Becker, W., et al. 2012, arXiv:1209.3114
Nandra, K., Laird, E. S., Adelberger, K., et al. 2005, MNRAS, 356, 568
Nandra, K., Laird, E. S., Aird, J. A., et al. 2015, ApJS, 220, 10
Pineau, F. X., Derriere, S., Motch, C., et al. 2017, A&A, 597, A89
Ranalli, P., Georgantopoulos, I., Corral, A., et al. 2015, A&A, 577, A121
Rosen, S. R., Webb, N. A., Watson, M. G., et al. 2016, A&A, 590, A1
Salvato, M., Buchner, J., Budavári, T., et al. 2018, MNRAS, 473, 4937
Schlafly, E. F., Meisner, A. M., & Green, G. M. 2019, ApJS, 240, 30
Shen, Y., Brandt, W. N., Dawson, K. S., et al. 2015, ApJS, 216, 4
Shen, Y., Hall, P. B., Horne, K., et al. 2019, ApJS, 241, 34
Smee, S. A., Gunn, J. E., Uomoto, A., et al. 2013, AJ, 146, 32
Tonry, J. L., Stubbs, C. W., Kilic, M., et al. 2012, ApJ, 745, 42
Watson, M. G., Schröder, A. C., Fyfe, D., et al. 2009, A&A, 493, 339
Wen, Z. L., Han, J. L., & Liu, F. S. 2012, ApJS, 199, 34
White, R. L., Becker, R. H., Helfand, D. J., & Gregg, M. D. 1997, ApJ,
Wright, E. L., Eisenhardt, P. R. M., Mainzer, A. K., et al. 2010, AJ, 140, 1868
York, D. G., Adelman, J., Anderson, J. E., et al. 2000, AJ, 120, 1579
```